Numerical Investigation of Intense Rainfall Effects on Coherent and Incoherent Slant-Path Propagation at K-Band and Above

Frank Silvio Marzano, *Senior Member, IEEE,* and Laura Roberti, *Member, IEEE,*

***Abstract*—A model investigation is carried out to analyze the impact of intense rainfall on slant-path microwave propagation, using a rainfall microphysical model. The effects are evaluated both for path attenuation, undergone by coherent radiation, and for multiple scattering phenomena, originating incoherent radiation along the path. Atmospheric spatial inhomogeneity is taken into account by considering a precipitating-cloud three-dimensional distribution, obtained from the numerical outputs of a microphysical cloud-resolving model. The electromagnetic propagation model is formulated by means of the radiative transfer theory, rigorously defining the forward coherent multiple scattering effect within this framework. The propagation model is applied both to simplified rain slabs and to vertically and horizontally inhomogeneous raining cloud structures in order to compare the impact of atmospheric models on coherent and incoherent propagation. Beacon frequencies between 20–50 GHz are considered together with elevation angles between 20° – 40° and surface rain rates from 1 to 100 mm/h. Appropriate sensitivity analysis parameters are defined to present and discuss the numerical results. The main conclusion of this numerical study is that the impact of the convective rainfall structure can be significant both in determining total attenuation and to quantify multiple scattering contribution to the received power. For intense rainfall, the use of a rain slab model can overestimate coherent attenuation and, at the same time, underestimate incoherent intensity. The analysis of realistic raining clouds structures reveals the significance of modeling the volumetric albedo of precipitating ice, particularly at V-band. Total path attenuation can strongly depend on the pointing direction of the receiving antenna due to the intrinsic variability of the precipitating cloud composition along the slant path. Coupling cloud-resolving models with radiative transfer schemes may be foreseen as a new approach to develop statistical prediction methods at Ka-band and above in a way analogous to that pursued by using weather-radar volume data.**

***Index Terms*—Cloud and rainfall modeling, earth–satellite millimeter-wave links, microwave propagation, multiple scattering effects, radiative transfer theory, rain attenuation.**

Manuscript received June 2, 2000; revised November 2, 2001. This work was supported in part by the Italian Space Agency (ASI) and in part by the European Commission (EC) under the Fifth-framework EURAINSAT project EVG2-2000-00522.

F. S. Marzano is with the Dipartimento di Ingegneria Elettrica, Universitá dell'Aquila, Monteluco di Roio, 67040 L'Aquila, Italy (e-mail: marzano@ing.univaq.it).

L. Roberti was with the Dipartimento di Elettronica, Politecnico di Torino, 10129 Turin, Italy. She is now with the British Telecom Laboratories, Martlesham Heath, Ipswich, IP5 3RE U.K. (e-mail: Laura.Roberti@bt.com).

Digital Object Identifier 10.1109/TAP.2003.811462

I. Introduction

In THE LAST decade space-earth link design has been strongly oriented to tackle with the optimization of communication systems with large-bandwidth, high availability, and low-fade margin [1], [2]. The request of larger channel capacity has lead to the exploration of channels at K-band and above. Beacon frequencies between 20 and 50 GHz have been theoretically and experimentally investigated in order to develop accurate radio-propagation models [3]–[4]. When using frequency bands above 20 GHz, the atmospheric fading due to clouds and rain, together with scintillation, can represent a strong impairment to the link budget design [5]. Intense rainfall, due to convective storms, can cause severe path attenuation of coherent radiation at K and above [6], [7].

The growing interest toward the accurate modeling and prediction of instantaneous rainfall path attenuation is justified by the emergence of effective countermeasure techniques to mitigate outage periods on a short-term basis (if not in near-real time) [5]. The estimate of instantaneous rainfall attenuation can be accomplished by adopting various models, essentially based on forward coherent single-scattering calculations and rain slab models [8]–[11]. In many circumstances these assumptions can result to be unrealistic [12], [13]. The role of precipitating ice scattering can be significant above 20 GHz so that neglecting its contribution can lead to an erroneous evaluation of the total path attenuation [14]. With respect to rain, ice spatial distribution can be highly variable and difficult to be micro-physically described.

A way to approach the characterization of precipitating clouds is to resort to the analysis of weather-radar volume data processed in such a way to retrieve rainfall spatial grid [12]. Polarimetric S-band radar techniques are suitable to this aim as the uncertainty of raindrop size distribution within each radar bin can be partially resolved and the identification of hydrometeor category along the range be possibly accomplished [13]. Inherent limitations of using radar data are due to measurement errors and to the difficulty to quantify precipitating ice amount. The recent availability of mesoscale cloud-resolving model simulations can also give an appealing chance to consider physically-consistent three-dimensional (3-D) atmospheric scenarios [15], [16]. Indeed, the spatial distribution of hydrometeor contents in liquid, frozen and melted phase can be obtained [15]. Inevitable ambiguities are associated to such 3-D models dependent on the assumptions adopted for describing the underlying cloud microphysics

and dynamics. Nevertheless, they represent a valuable data sources which could be used to carry out model analyses and to develop rainfall prediction techniques in the same way as already accomplished using radar data.

Most approaches to microwave attenuation modeling have been based on the assumption of negligible incoherent effects due to rain multiple scattering [17]. This choice allows one to simplify the propagation problem by considering only the extinction mechanism for computing the total path attenuation. Several studies have been carried out in the last twenty years to understand and quantify the rain incoherent effects [18]–[26]. These approaches have been based on both the Twerskii-Foldy multiple scattering theory and on the radiative transfer (RT) theory [27]. The latter theoretical framework enables the evaluation of all orders of scattering, even though formulated only for specific intensity of the electromagnetic (e.m.) field.

Referring to a uniform rain slab where a plane wave is normally incident, that is to line-of-sights with elevation angles (above the horizon) of 90° [25], [28], the basic conclusion of most works is that rainfall multiple scattering is negligible in the microwave and millimeter-wave links for rain rates up to 150 mm/h [28]. Indeed, most earth–satellite links generally are operated with much lower elevation angles [2], [4], [29]. Available numerical results for slant-path microwave propagation have showed that, for intense precipitation and frequencies above 20 GHz, the multiple scattering effects of a rain slab can be significant for path attenuation larger than 100 dB [22], [24].

The coupling of a propagation model, which includes multiple scattering of hydrometeors in different phases, with a numerical cloud-resolving model simulation can open the possibility of a thorough analysis of coherent and incoherent propagation properties including the impact of spatially inhomogeneous precipitation [26]. The capability to model (and possibly predict) the additional receiver noise, due to precipitating-cloud incoherent effects, can be a valuable tool for a more accurate link budget design. This is especially true if an adaptive processing of the instantaneous received intensity, and not its average (coherent) value, has to be taken into account [5].

In this work, a model investigation is carried out to evaluate the impact of intense rainfall and ice spatial distribution upon slant-path microwave coherent and incoherent propagation along earth–satellite links in the 20–50-GHz band. In Section II, some theoretical considerations are illustrated in order to frame the RT theory within the multiple scattering theory and to highlight its basic assumptions. Incoherent and forward coherent multiple scattering are discussed and rigorously defined within the RT framework. The RT propagation model is described together with the solution method based on the application of a finite-element technique. In Section III the atmospheric model is illustrated by using the 3-D outputs of a numerical simulation of a detailed microphysical cloud model. Cross sections of single-scattering parameters are shown to better interpret the subsequent RT outputs. Sensitivity analysis parameters are defined in order to effectively plot and discuss the numerical results. The latter are exposed in Section IV, following the idea of an increasing complexity of the cloud geometry for RT computations. First, an equivalent rain slab is derived from the cloud three-dimensional grid, then vertically inhomogeneous (plane-parallel) raining cloud structures are extracted, and finally vertically and horizontally inhomogeneous cloud structures are analyzed. The goal of this inter-comparison analysis is to underline the importance of considering cloud realistic geometries together with the effect of intense rainfall on slant paths. Final considerations on this model analysis are eventually given in Section V.

II. Propagation Model

Atmospheric precipitation is constituted by hydrometeors in ice, liquid, and mixed phase [15], [17], [27]. Rainfall is usually modeled as a continuous medium (background) filled by randomly distributed discrete scatterers. A coherent signal crossing such a medium is affected by the random nature of the medium itself. At the receiver, the partially-coherent received field $\Psi(\mathbf{r})$ can be divided into an average $\langle\Psi(\mathbf{r})\rangle$ and a fluctuating $\Psi_f(\mathbf{r})$ part (with a zero mean), that is $\Psi(\mathbf{r}) = \langle\Psi(\mathbf{r})\rangle + \Psi_f(\mathbf{r})$, where $\mathbf{r}$ is the position vector [30]. The average field is usually called the "coherent" field, while the fluctuating one is called the "incoherent" field. In this analysis we will consider only scalar fields thus avoiding the description of the medium effects on the polarization state of the field.

A. Theoretical Considerations

Several methods have been devised in the last two decades to analytically formulate the problem and find approximate solutions for the scattered field. Excellent review works describe these efforts [17], [23], [24], [27]. A well known approach is the one described by the integral equation of Twerskii-Foldy for the coherent field [31]. Supposing a low particle density and a negligible particle size so that the location and the characteristics of each scatterers are independent of the location and characteristics of other scatterers (thus simplifying the statistical averaging), it can be shown that $\langle\Psi(\mathbf{r})\rangle$ behaves locally as a plane wave and satisfies the Helmholtz homogeneous equation $(\nabla^2 + K^2)\langle\Psi(\mathbf{r})\rangle = 0$, where the effective (complex) propagation constant K is given by [23], [30]

$$K = K_r - jK_j = k + \frac{2\pi}{k}\int_0^\infty f(0,D)N(D)dD. \quad (1)$$

In (1) K_r and K_j are the real and the imaginary part of K, k is the wave number, $f(\Omega_s, D)$ is the complex scattering amplitude of the single particle dependent on the scattering solid angle Ω_s and on the particle diameter D, and $N(D)$ is the particle size distribution per unit volume. Obviously, the term $f(0,D)$ indicates forward scattering amplitude. We can apply the "forward scattering theorem" to the forward-scattering amplitude $f(0,D)$ and re-express K_j as follows:

$$K_j = \mathrm{Im}[K] = \frac{1}{2}\mathrm{Im}\left[\frac{4\pi}{k}\int_0^\infty f(0,D)N(D)dD\right] = \frac{k_e}{2} \quad (2)$$

where k_e is the volumetric extinction coefficient of the medium.

Considering that the solution for the coherent intensity $|\langle\Psi(\mathbf{r})\rangle|^2$ is straightforward in an uniform medium, in this

case the transmission coefficient T of the coherent field can be written as follows:

$$T(\mathbf{r}_A, \mathbf{r}_0) = \frac{|\langle\Psi(\mathbf{r}_A)\rangle|}{|\langle\Psi(\mathbf{r}_0)\rangle|} = \left|e^{-j(K-k)s}\right| = e^{-\frac{k_e}{2}s} \quad (3)$$

where the coherent field is supposed to be incident at $\mathbf{r} = \mathbf{r}_0$ with amplitude $|\langle\Psi(\mathbf{r}_0)\rangle|$, while $\mathbf{r}_A$ is the position vector at the receiving antenna location and s the propagation coordinate within the medium. It was pointed out by Olsen [23] that, by expanding the exponent of the transmission coefficient T along the propagation coordinate s, the terms involving $f^n(0, D)$ account exactly for the coherent contribution of all forward multiple scattering processes of order n. The denomination "forward coherent" multiple scattering was then introduced to indicate that the multiple scattering paths between the scatterers have all an in-phase component in the forward direction.

If we deal with the intensity of the received field, we can deduce that the total intensity $\langle|\Psi(\mathbf{r})|^2\rangle$ is the sum of the coherent intensity $|\langle\Psi(\mathbf{r})\rangle|^2$ and incoherent intensity $\langle|\Psi_f(\mathbf{r})|^2\rangle$, that is $\langle|\Psi(\mathbf{r})|^2\rangle = |\langle\Psi(\mathbf{r})\rangle|^2 + \langle|\Psi_f(\mathbf{r})|^2\rangle$ [24]. A set of two integral equations for the total intensity $\langle|\Psi(\mathbf{r})|^2\rangle$ has been derived by Twerskii. To our knowledge analytical solutions to the these integral equations have not appeared in literature so far, even though several approximate solutions have been proposed and compared with experimental data [27].

From the Twerskii integral equations for the total intensity and, more generally, for the correlation function of the total field $\Psi(\mathbf{r})$, the integro-differential equation of radiative transfer can be derived under some hypotheses [30]. The most important of the latter is that the correlation function $\Gamma(\mathbf{r}, \mathbf{r}_\mathrm{d})$ is a slowly varying function with $\mathbf{r}$, being $\mathbf{r}_\mathrm{d}$ the correlation distance vector. If this assumption holds (as for atmospheric precipitation crossed by microwave radiation), the total intensity can be expressed in a mathematical form through the specific intensity $I(\mathbf{r}, \mathbf{s})$

$$\left\langle|\Psi(\mathbf{r})|^2\right\rangle = \Gamma(\mathbf{r}, 0) = \int_{4\pi} I(\mathbf{r}, \mathbf{s}) d\Omega \quad (4)$$

where $\mathrm{d}\Omega$ is a differential solid angle in the direction of the unit vector $\mathbf{s}$. If the intensity $\langle|\Psi(\mathbf{r})|^2\rangle$ is expressed in [W m^{-2}Hz^{-1}], clearly $I(\mathbf{r}, \mathbf{s})$ is given in [W m^{-2}Hz^{-1}sr^{-1}]. Using (4), the Twerskii integral equations can be converted into the following integro-differential equation for the specific intensity $I(\mathbf{r}, \mathbf{s})$ [30]:

$$\frac{d}{ds} I(\mathbf{r}) = -k_e I(\mathbf{r}, \mathbf{s}) + \int_{4\pi} k_d(\mathbf{s}, \mathbf{s}') I(\mathbf{r}, \mathbf{s}') d\Omega' \quad (5)$$

where $k_d(\mathbf{s}, \mathbf{s}')$ is the differential volumetric scattering coefficient, defined by

$$k_d(\mathbf{s}, \mathbf{s}') = \int_0^\infty |f(\mathbf{s}, \mathbf{s}', D)|^2 N(D) dD. \quad (6)$$

We can easily recognize that (5) has the form of the classical RT equation [27], [33]. Its validity is generally ensured for nondense nontenuous scattering media so that, in practice, (5) holds for a medium having a volumetric density fraction less few percentage; the atmosphere with precipitation satisfies these assumptions [34], [35]. Notice that in (5) phase effects (field interference) are neglected so that we are allowed to carry out the sum of the intensity due to each atmospheric contribution. As usual in the context of wave propagation, in the second member of (5) we have neglected the pseudo-source term due to the thermal emission of the medium [27], [32], [35].

B. Forward Coherent and Incoherent Multiple Scattering

In analogy to field amplitude, we can decompose I into a coherent part I_c and incoherent part I_i, that is from (4)

$$\left\langle|\Psi(\mathbf{r})|^2\right\rangle = |\langle\Psi(\mathbf{r})\rangle|^2 + \left\langle|\Psi_f(\mathbf{r})|^2\right\rangle = \int_{4\pi} I_c(\mathbf{r}, \mathbf{s}) d\Omega + \int_{4\pi} I_i(\mathbf{r}, \mathbf{s}) d\Omega \quad (7)$$

with $I(\mathbf{r}, \mathbf{s}) = I_c(\mathbf{r}, \mathbf{s}) + I_i(\mathbf{r}, \mathbf{s})$. Thus, substituting (7) in (5) gives rise to the following set of equations for the coherent and incoherent intensity, respectively:

$$\begin{cases} \frac{d}{ds} I_c(\mathbf{r}) = -k_e I_c(\mathbf{r}, \mathbf{s}) & \text{(8a)} \\ \frac{d}{ds} I_i(\mathbf{r}) = -k_e I_i(\mathbf{r}, \mathbf{s}) + \int_{4\pi} k_d(\mathbf{s}, \mathbf{s}') I_i(\mathbf{r}, \mathbf{s}') d\Omega' \\ \qquad + \int_{4\pi} k_d(\mathbf{s}, \mathbf{s}') I_c(\mathbf{r}, \mathbf{s}') d\Omega'. & \text{(8b)} \end{cases}$$

The interpretation of (8a) is such that the coherent specific intensity is decreased by extinction due to the medium particle distribution. This is the reason why I_c is also called reduced intensity [22]. Being $I_{c0}(\mathbf{r}_0, \mathbf{s})$ the incident coherent intensity at $\mathbf{r} = \mathbf{r}_0$, the solution of (8a) for I_c is simply given by

$$I_c(\mathbf{r}_A, \mathbf{s}) = I_{c0}(\mathbf{r}_0, \mathbf{s}) e^{-\tau(\mathbf{r}_0, \mathbf{r}_A)} = I_{c0}(\mathbf{r}_0, \mathbf{s}) e^{-\int_0^{s_A} k_e(s') ds'} \quad (9)$$

where $\mathbf{r}_\mathrm{A}$ is the position vector at the antenna location, $\tau(\mathbf{r}_0, \mathbf{r}_\mathrm{A})$ is the optical thickness between $\mathbf{r}_0(\mathbf{s}' = 0)$ and $\mathbf{r}_\mathrm{A}$ (where $s' = \mathrm{s_A}$).

It is important to stress that (9), also referred to as the Beer–Bouguer–Lambert law [32], is identical to the solution of the Twerskii differential equation for the coherent intensity. This can be simply shown by expressing for the intensity transmission coefficient in case of a uniform scattering layer. It holds

$$T^2(\mathbf{r}_A, \mathbf{r}_0) = \frac{|\langle\Psi(\mathbf{r}_A)\rangle|^2}{|\langle\Psi(\mathbf{r}_0)\rangle|^2} = \frac{\int_{4\pi} I_c(\mathbf{r}_A, \mathbf{s}) d\Omega}{\int_{4\pi} I_c(\mathbf{r}_0, \mathbf{s}) d\Omega} = e^{-k_e s}. \quad (10)$$

Comparing (10) with (3), the previously mentioned "forward coherent" multiple scattering results to be fully described by (8) within the RT theory.

From (8b), we also realize that the incoherent specific intensity, also called diffuse intensity, is created within the medium by incoherent multiple scattering phenomena (second term on the right side) and by the equivalent source due to the incident coherent intensity (third term on the right side).

Proper boundary conditions at $\mathbf{r} = \mathbf{r}_0$ and $\mathbf{r} = \mathbf{r}_\mathrm{A}$ should be coupled with (8). Moreover, in order to take into account the receiver characteristics, we can introduce the antenna equivalent

area A_e so that the received power $P_{\rm R}(\mathbf{r}_{\rm A}, \mathbf{s}_{\rm A})$ at $\mathbf{r} = \mathbf{r}_{\rm A}$ along the antenna orientation unit-vector $\mathbf{s}_A$ can be expressed as [27]

$$\begin{aligned} P_R(\mathbf{r}_A, \mathbf{s}_A) &= P_{Rc}(\mathbf{r}_A, \mathbf{s}_A) + P_{Ri}(\mathbf{r}_A, \mathbf{s}_A) \\ &= \int_{4\pi} A_e(\mathbf{s}_A, \mathbf{s}) I_c(\mathbf{r}, \mathbf{s}) d\Omega \\ &\quad + \int_{4\pi} A_e(\mathbf{s}_A, \mathbf{s}) I_i(\mathbf{r}, \mathbf{s}) d\Omega \end{aligned} \tag{11}$$

where $P_{\rm R}$ has been split into a coherent $P_{\rm Rc}$ and incoherent $P_{\rm Ri}$ component.

C. Radiative Transfer Model

The solution of (8b) is not an easy task, especially if considering a three-dimensional geometry of the scattering medium [36]–[38]. Under the assumption of a plane-parallel medium (horizontally stratified), the RT equation can be simplified and expressed using the coordinates z (distance), θ (zenithal angle), and ϕ (azimuthal angle).

Let us introduce, as a boundary condition, a collimated beam along the direction $\mathbf{s}_{\rm A}$ incident at the top of the medium for $\mathrm{z} = 0$ (i.e., $\mathbf{r} = \mathbf{r}_0$), that is a coherent incident plane-wave whose specific intensity is given by

$$\begin{aligned} I_{c0}(\mathbf{r}_0, \mathbf{s}_A) &= I_{c0}(z = 0, \mathbf{s}_A) \\ &= F_0 \delta(\Omega - \Omega_0) \\ &= F_0 \delta(\mu - \mu_0) \delta(\phi - \phi_0) \end{aligned} \tag{12}$$

where $\mathbf{F}_0$ is the incident flux (power) density, $\mu = \cos\theta$, and $\delta(\boldsymbol{\Omega} - \boldsymbol{\Omega}_0)$ is a solid-angle delta function with $\boldsymbol{\Omega}$ and $\boldsymbol{\Omega}_0$ are the unit vectors in the direction $\mathbf{s} = (\theta, \phi)$ and $\mathbf{s}_A = (\theta_0, \phi_0)$, respectively. Notice that $I_i(\mathbf{r}_0, \mathbf{s}) = 0$.

Using the optical thickness as an equivalent distance coordinate and by substituting (12) in (8), the latter equation for the incoherent specific intensity in a plane-parallel medium becomes [27], [32]

$$\begin{aligned} \mu \frac{d}{d\tau} I_i(\tau, \mu, \phi) = &- k_e I_i(\tau, \mu, \phi) \\ &+ \frac{w(\tau)}{4\pi} \int_{4\pi} p(\tau, \mu, \phi, \mu', \phi') I_i(\tau, \mu, \phi) d\Omega' \\ &+ \frac{w(\tau)}{4\pi} p(\tau, \mu, \phi, \mu_0, \phi_0) F_0 e^{\frac{-\tau}{\mu_0}} \end{aligned} \tag{13}$$

where $\mu_0 = \cos\theta_0$ and the volumetric albedo w is defined by $w = k_s/k_e$, being k_s the volumetric scattering coefficient, while the scattering phase function p is given by $p(\mu, \phi, \mu', \phi') = 4\pi k_d(\mu, \phi, \mu', \phi')/k_s$. Notice that the definition of p in (13) is such that it is normalized to 4π with respect to the solid angle. It holds $k_e = k_a + k_s$ with k_a the volumetric absorption coefficient so that $0 \leq w \leq 1$.

The RT equation in the form of (13) can be numerically solved by adopting various techniques [22], [39]. In this work the RT equation is solved by using a recently developed finite-element method (FEM), which has shown to be accurate and quickly converging [39], [40]. For the FEM solution, the specific intensity is represented by a Fourier cosine series, that is

$$I_i(\tau, \mu, \phi) = \sum_{m=0}^{M} I^m(\tau, \mu) \cos\left[m(\phi - \phi_0)\right]. \tag{14}$$

Using (14), the integro-differential equation in (13) splits up in $\mathrm{M} + 1$ independent equations, one for each harmonic $I^m(\tau, \mu)$. In accordance to FEM, the solution for each $I^m(\tau, \phi)$ is searched in the form [41]

$$I^m(\tau, \mu) = \sum_{k=1}^{2N} b_k^m(\mu) I_k^m(\tau) \tag{15}$$

where $b_k^m(\mu)$ with $k = 1$, 2N is a system of basis functions which are nonzero only in a finite interval. A set of triangular basis functions can be chosen. Substituting into (13) and projecting onto the conjugate space, that is using FEM in the Galerkin form, a system of coupled differential equations is found for each harmonic, which can be eventually solved by linear algebra methods.

As a particular case of the general solution, we can consider the first-order scattering solution which represents a multiple scattering approximation in the iterative solution method of successive orders of scattering. It is obtained by considering as a source function in (13) only the term relative to the incident reduced intensity thus taking into account only the intensity due to waves scattered once [27]. By assuming that there is no incoherent downward and upward intensity at the top and at the bottom of the layered atmosphere, respectively, the transmitted first-order-scattering incoherent specific intensity $I_{\rm iFS}$ for $\tau = \tau_{\rm A}$ (i.e., $\mathbf{r} = \mathbf{r}_{\rm A}$) and along the incident direction Ω_0 [see (12)] is expressed by [27], [32]

$$I_{iFS}(\tau_A, \mu_0, \phi_0) = \frac{w \tau_A F_0}{4\pi \mu_0} p(\mu_0, \phi_0, \mu_0, \phi_0) e^{\frac{-\tau_A}{\mu_0}}. \tag{16}$$

A recursive relationship can be easily deduced to provide solutions for higher orders of scattering.

III. Atmospheric Model and Definitions

The radiative transfer computations in this study refer to physically-consistent cloud profiles obtained from the mesoscale cloud-resolving microphysical-dynamical 3-D model, called Goddard cumulus ensemble (GCE) and developed by Tao *et al.* [15]. In order to simulate current propagation links and experiments, radiative transfer computations have been performed at four different frequencies between the K- and V-band, i.e. at 19.7, 29.6, 39.6, and 49.5 GHz (hereafter, also called 20, 30, 40, and 50 GHz for brevity). These beacon frequencies have been chosen by basically collecting the channel frequencies of the OLYMPUS and ITALSAT satellites [4], [29].

A. Raining Cloud Microphysical Model

The cloud-resolving model domain consists of 64 by 64 pixels, that is 96 by 96 km with a horizontal resolution

of 1.5 km, sampled every 15 min during the evolution of the simulated storm. A single time-step, representing a mature squall line over ocean in the tropical region, has been chosen for this numerical study. Even though referred to a specific cloud event, the ensemble of cloud vertical profiles can statistically represent a large variety of convective cloud structures with a freezing level between 4.5 and 5 km.

Each pixel of the cloud-grid simulation comprises 21 vertical layers from the surface to a height of 18 km with a vertical resolution of about 1 km. The cloud model specifies the height, pressure, temperature, relative humidity, cloud water, rain water, ice graupel (precipitating ice), ice crystals, and snow contents of each grid-cell. Rain, graupel, and snow mass densities are fixed to 1.0, 0.4, and 0.1 g cm^{-3}, respectively. All hydrometeors' shapes have been assumed to be spherical, even though this assumption might be not appropriate especially for snow particles. Being the simulated storm basically convective, no mixed-phase hydrometeors (as those typical of a melting layer just below the freezing level in stratiform rain) have been considered here. Surface rain rate has been derived by means of a rainfall model depending on the terminal velocity parameterization at each grid point [15].

Cloud liquid and ice crystals have been considered to be monodisperse with a characteristic diameter of 20 μm. An inverse-exponential hydrometeor size distribution (HSD) has been used for snow, rain and graupel. The general HSD form is the following $N(D) = N_0 \exp(-\Lambda D)$, with the "logarithmic slope" Λ of $ln[N(D)]$ given by $\Lambda = (\pi \rho N_0 / L)^{0.25}$, being L the hydrometeor equivalent water content in g m^{-3} [15]. The "intercept" N_0 of $ln[N(D)]$ is constant and equal to 0.08 cm^{-4} for rain as in the Marshall–Palmer distribution, to 0.04 cm^{-4} for snow and graupel.

It is worth mentioning that the assumed HSD is variable with height if a vertical profile of L is assigned, as in the case of a cloud-resolving model. Using an already available hydrometeor content L necessarily imposes one of the two HSD parameters (the alternative could be to fix Λ and to derive N_0). The dependence of the logarithmic slope Λ on L governs the concentration of larger drops (with respect to smaller ones) which significantly impact hydrometeor scattering properties. This causes significant differences of cloud-model HSDs with respect to conventional HSDs, such as the Marshall–Palmer or the Laws–Parsons one [10].

Atmospheric gaseous absorption has been computed by means of the Liebe model [42]. Mie theory has been used for evaluating the single-scattering parameters of spherical hydrometeors [25]. The Heney–Greenstein (HG) approximation has been assumed for the scattering phase function $p(\mu, \phi, \mu', \phi')$, that is [43]

$$p(\mu, \phi, \mu', \phi') = p(\mathbf{s}, \mathbf{s}') = p(\Omega_s) = \frac{1 - g^2}{(1 - g^2 - 2g\mu_s)^{\frac{-3}{2}}} \tag{17}$$

where g is the volumetric asymmetry factor and $\mu_s = \mathbf{s} \cdot \mathbf{s}' = \cos(\Omega_s)$ is the cosine of the scattering solid angle. The HG choice enables an easy expansion of the phase function in terms of Legendre polynomials since the expansion moments are powers of the volumetric asymmetry factor g. The latter, proportional to the first moment of the phase-function expansion, is given by [32], [43]

$$g = \frac{1}{4\pi} \int_{4\pi} p(\mathbf{s}, \mathbf{s}') \mathbf{s} \cdot \mathbf{s}' d\Omega_s = \frac{\int_{4\pi} p(\mathbf{s}, \mathbf{s}') \mu_s d\Omega_s}{\int_{4\pi} p(\mathbf{s}, \mathbf{s}') d\Omega_s}. \tag{18}$$

The asymmetry factor g has an interesting interpretation as it represents the averaged forward scattering (i.e., $\mathbf{s} \cdot \mathbf{s}' > 0$) minus the backward scattering ($\mathbf{s} \cdot \mathbf{s}' < 0$) of the particle ensemble. From (18), it holds $-1 \leq g \leq 1$. For isotropic scattering $g = 0$, while g tends to 1 (-1) as the diffraction peak of the phase function becomes increasingly sharpened in the forward (backward) direction.

An unpolarized incoming plane wave has been supposed obliquely incident at the top boundary in z $= 0$. A perfectly absorbing surface has been considered: this assumption is not restrictive since only the down going radiation has to be computed and the microwave emissivity of the ground is generally close to 1 [12].

Fig. 1 shows a GCE vertical cross sections of cloud, rain, and graupel equivalent water contents, produced by the cloud model, together with the associated surface rain rate. This section refers to the line y $= 48$ which corresponds to the most intense convective portion of the storm.

Values of rain and ice graupel up to 7 and 5 g m^{-3} are observed around x $= 30$ km where the instantaneous surface rain rate can reach about 150 mm/h. Rain spatial distribution appears to be inhomogeneous both vertically and horizontally. The freezing level is at about 5 km, as typical in a tropical summer environment. Precipitating ice graupel is mostly concentrated above the freezing level, while cloud liquid is reduced where rain water is generated by coalescence and fallout processes. Maxima of surface rain rate are well correlated with rain and ice vertical distribution.

By performing the single-scattering computations as described above, we can associate to the raining cloud cross-section, shown in Fig. 1, the corresponding section of the fundamental optical parameters inputs to the RT equation. The top panels of Fig. 2 show the vertical cross-section of the specific attenuation $A_{\rm s}$ in dB/km (proportional to k_e through $A_s = 4.343\ k_e$) at 20 and 50 GHz. At K-band, $A_{\rm s}$ is less than 15 dB/km and, by comparing with hydrometeor spatial distribution, it is basically due to raindrops. However, when going up to 50 GHz, $A_{\rm s}$ can even reach values of 40 dB/km with a predominance of rain contribution, but with a graupel impact above the freezing level of the order of 10 dB/km.

By analyzing (13), the multiple scattering source term is weighted by the volumetric albedo w. Middle panels of Fig. 2 show the vertical cross-section of w at 20 and 50 GHz. Before commenting the figure, it should be bear in mind that, due to its definition, w is relatively small for high absorbing particles (as raindrops), while relatively large for highly scattering particles (as ice graupel). Indeed, numerical results confirm that values of w up to 0.9 are found only above the freezing level where ice graupel is present. As expected, w increases with frequency due to the fact that, when raising the frequency (i.e., decreasing the wavelength), smaller particles begin to contribute to scattering more and more significantly [43].

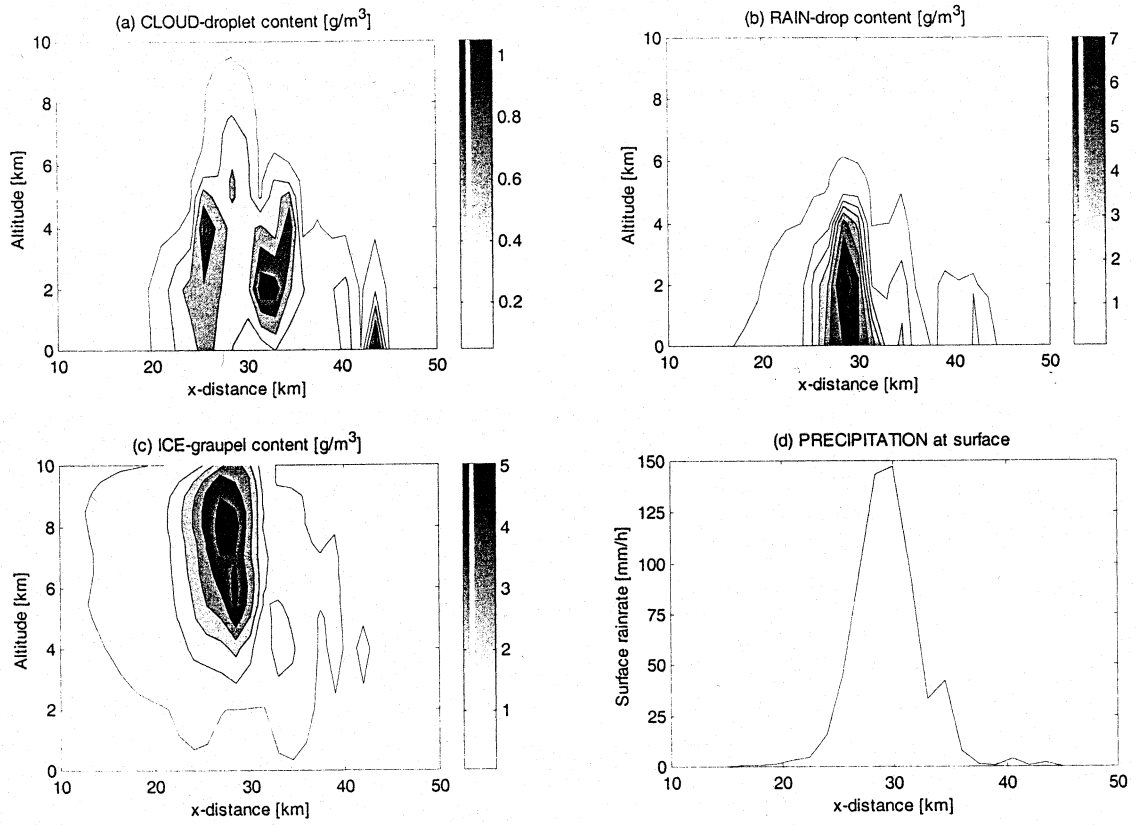

Fig. 1. Vertical cross sections of: (a) cloud, (b) rain, (c) graupel, and (d) equivalent water contents [g/m^3] together with the surface rain rate R, produced by the GCE cloud-resolving model. The section refers to the line y = 48 for the time step t = 210, corresponding to the mature stage of the simulated squall line. Values greater than 0.05 g/m^3 are plotted with contour increments of 0.25 g/m^3 for cloud and snow, and 1 g/m^3 for rain and graupel.

A question may be raised concerning the prevailing direction of scattering processes within the raining cloud. The answer can be obtained by looking at the volumetric asymmetry factor g. Bottom panels of Fig. 2 show the vertical cross-section of g at 20 and 50 GHz. Values of g are higher where ice graupel is present and they are always greater than zero within the cloud, meaning that forward scattering is giving the major contribution. Factor g increases with frequency, as expected from the Mie theory since the scattered radiation is more and more peaked in the forward direction. Values of g are generally less than 0.15 in the 20–50 GHz band. This aspect indicates that, even though forward scattering is the prevailing process, we cannot neglect specific intensity scattered in directions other that the forward one when the albedo is sufficiently high.

B. Definitions for Numerical Analysis

The detection of multiple scattering effects is strongly dependent on the directivity of the receiving antenna. This consideration is easily justified by looking at (11) where the received power is given by the incoming specific intensity weighted by the equivalent area pattern. In order to take it into account, we have used a Gaussian azimuthally isotropic pattern function, as proposed in [20]. From the "reciprocity" theorem for a receiving antenna, (11) can be rewritten as

$$P_R(\mathbf{r}_A,\mathbf{s}_A)=\int_{4\pi} A_e(\mathbf{s}_A,\mathbf{s})I(\mathbf{r},\mathbf{s})d\Omega$$

$$=\frac{\lambda^2}{4\pi}\int_{4R} G_M G_n(\mathbf{s}_A,\mathbf{s})I(\mathbf{r},\mathbf{s})d\Omega \qquad (19)$$

where G_{M} is the maximum antenna gain and G_{n} is the normalized (to the maximum) antenna gain pattern function, modeled as [28]

$$G_n(\mathbf{s}_A,\mathbf{s})=G_n(\theta,\theta_0)=\ e^{\ln\left(\frac{1}{2}\right)\left[\frac{\sin(\theta-\theta_0)}{\sin(\theta_A)}\right]^2} \qquad (20)$$

being θ_0 the pointing zenithal direction (coincident with the incident one of the collimated beam) and θ_{A} is the semi-angle of the half-power beamwidth. If the specific intensity $I(\mathbf{r}_{\mathrm{A}},\mathbf{s})$ is assumed to be uniform within the antenna beamwidth, for highly directive antennas (19) yields $P_{\mathrm{R}}(\mathbf{r}_{\mathrm{A}},\mathbf{s}_{\mathrm{A}}) \cong (\lambda^2/4\pi)G_{\mathrm{M}}I(\mathbf{r}_{\mathrm{A}},\mathbf{s})(\pi\theta_{\mathrm{A}}^2)$, which is the approximation used in [22]. Notice that we do not model here the antenna noise temperature due to rainfall along the path [36], [38].

Before defining the basic analysis parameters, we can decompose the total attenuation into a coherent and incoherent component in analogy to (7). Incoherent effects tend to increase the received power with respect to considering the coherent part only. This means that incoherent attenuation is negatively defined with respect to total optical thickness $\tau_{\mathrm{A}}=\tau(\mathbf{r}_0,\mathbf{r}_{\mathrm{A}})$. From (7) and (9) in a plane-parallel medium, we have

$$I(\mathbf{r}_A,\mathbf{s})=I_c(\mathbf{r}_A,\mathbf{s})+I_i(\mathbf{r}_A,\mathbf{s})$$
$$=I_{c0}(\mathbf{r}_0,\mathbf{s})e^{\frac{-\tau_{\mathrm{A}}}{\mu_0}}+I_i(\mathbf{r}_A,\mathbf{s}). \qquad (21)$$

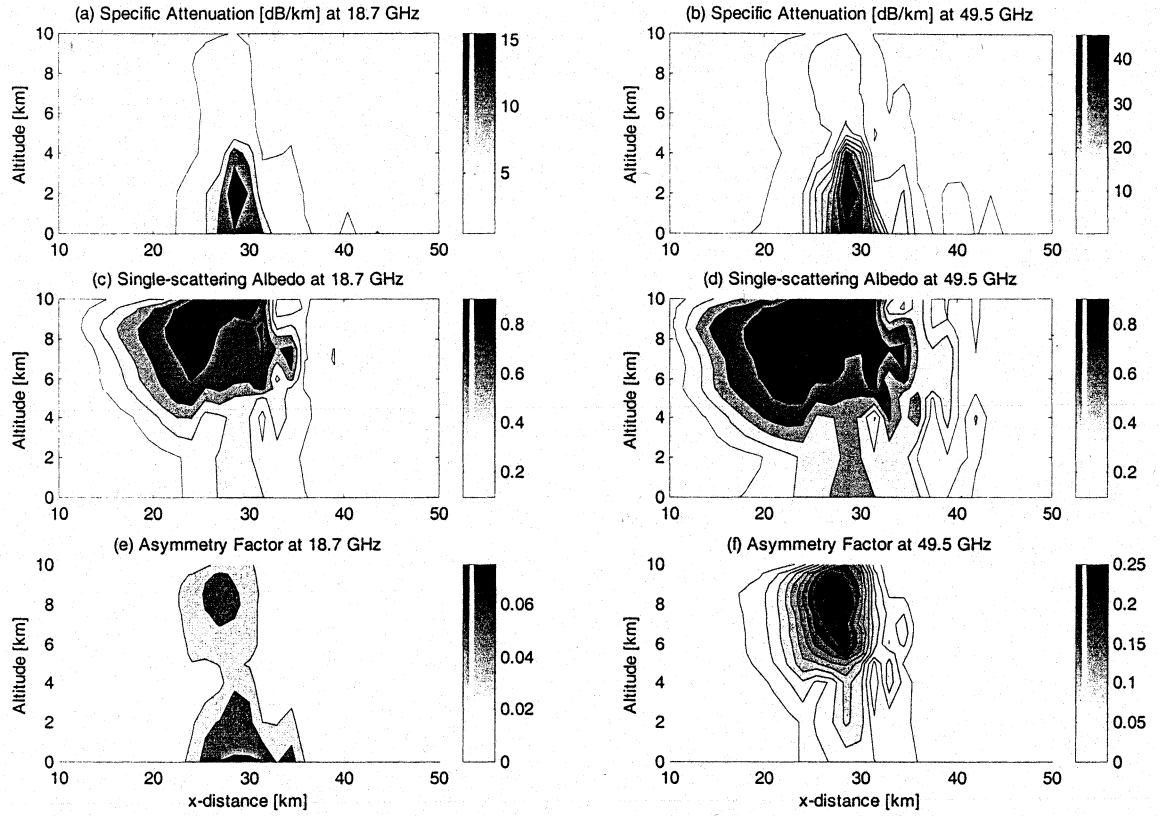

Fig. 2. Vertical cross sections (derived from Fig. 1) of: 1) specific attenuation A_s at (a) 19.7 GHz and (b) 49.5 GHz, hereafter also called 20, 30, 40, and 50 GHz, respectively (values greater than 0.5 dB/km are plotted with contour increments of 5 dB/km); 2) volumetric albedo w, defined in (18), at (c) 20 GHz and (d) 50 GHz (values greater than 0.1 are plotted with contour increments are of 0.2); and 3) volumetric asymmetry factor g, defined in (30), at (e) 20 GHz and (f) 50 GHz (contour increments are of 0.025).

By introducing an "incoherent" (negative) optical thickness $\tau_{\mathrm{A}i}$ such that

$$I_i(\mathbf{r}_A, \mathbf{s}) \equiv I_{c0}(\mathbf{r}_0, \mathbf{s}) e^{\frac{\tau_{Ai}}{\mu_0}} \tag{22}$$

and by defining a total optical thickness $\tau_{\mathrm{At}} \equiv \tau_{\mathrm{A}} - \tau_{\mathrm{Ai}}$, from (21) we can obtain an explicit expression for τ_{Ai}

$$\tau_{Ai} = \tau_A - \tau_{At} = \frac{1}{\mu_0} \ln \left[\frac{I(\mathbf{r}_A, \mathbf{s})}{I_{c0}(\mathbf{r}_0, \mathbf{s})} - e^{\frac{-\tau_A}{\mu_0}} \right]. \tag{23}$$

The following definitions are now introduced to better synthesize the numerical results of the next section.

1) *Coherent attenuation* A_{c} in decibels:

$$A_c = -10 \log \left[\frac{P_{Rc}(\mathbf{r}_A, \mathbf{s}_A)}{P_{R0}(\mathbf{r}_0, \mathbf{s}_A)} \right] = 4.343 \frac{\tau_A}{\mu_0} \tag{24}$$

where $P_{\mathrm{R0}}(\mathbf{r}_0, \mathbf{s}_A)$ is the incident power at the top-of-the-atmosphere due to the satellite transmitter. Since in (12) the incident intensity has been assumed to be collimated, from (19) it is obtained $P_{\mathrm{R0}}(\mathbf{r}_0, \mathbf{s}_A) = (\lambda^2/4\pi)\mathrm{G_T}F_0$, with $\mathrm{G_T}$ the satellite antenna transmitting gain in the pointing direction Ω_o. For simplicity, we have hereafter assumed $\mathrm{G_T} = \mathrm{G_M}$.

2) *Total attenuation* A_{t} in decibels:

$$A_t = -10 \log \left[\frac{P_R(\mathbf{r}_A, \mathbf{s}_A)}{P_{R0}(\mathbf{r}_0, \mathbf{s}_A)} \right] \tag{25}$$

which represents the total attenuation due both to multiple scattering and extinction. Neglecting the radiation pattern effects, it approximately holds $\mathrm{A_t} \cong 4.343\, \tau_{\mathrm{At}}/\mu_0$ so that $\mathrm{A_t} \leq \mathrm{A_c}$ due to the negative contribution of incoherent attenuation [see (22) and (23)].

3) *Incoherent-to-total attenuation ratio* ρ_{IT} in percent:

$$\rho_{\mathrm{IT}} = 100 \left[\frac{A_c - A_t}{A_t} \right] \tag{26}$$

which is a measure of the (negative) incoherent effects with respect to the total ones. Again, by neglecting the radiation pattern integration, it approximately holds $\rho_{\mathrm{IT}} \cong \tau_{\mathrm{Ai}}/\tau_{\mathrm{At}}$.

4) *Total-to-first-order-scattering attenuation ratio* ρ_{TF} in percent:

$$\rho_{\mathrm{TF}} = 100 \left[\frac{A_t}{A_{\mathrm{tFS}}} \right] = 100 \left[\frac{A_t}{-10 \log \left(\frac{P_{\mathrm{RFS}}(\mathbf{r}_A, \mathbf{s}_A)}{P_{\mathrm{R0}}(\mathbf{r}_0, \mathbf{s}_A)} \right)} \right] \tag{27}$$

where A_{tFS} in decibels is the first-order-scattering total attenuation being $P_{\mathrm{RFS}}(\mathbf{r}_{\mathrm{A}}, \mathbf{s}_{\mathrm{A}})$ given by (18) and $I(\mathbf{r}_{\mathrm{A}}, \mathbf{s}) = I_{\mathrm{c}}(\mathbf{r}_{\mathrm{A}}, \mathbf{s}) + I_{\mathrm{iFS}}(\mathbf{r}_{\mathrm{A}}, \mathbf{s})$ and I_{iFS} obtained from (16).

5) *Incoherent power discrimination* (IPD) in decibels:

$$\begin{aligned} \mathrm{IPD} &= 10 \log \left[\frac{P_{Rc}(\mathbf{r}_A, \mathbf{s}_A)}{P_{Ri}(\mathbf{r}_A, \mathbf{s}_A)} \right] \\ &= 10 \log \left[\frac{P_{Rc}(\mathbf{r}_A, \mathbf{s}_A)}{P_R(\mathbf{r}_A, \mathbf{s}_A) - P_{Rc}(\mathbf{r}_A, \mathbf{s}_A)} \right] \end{aligned} \tag{28}$$

which is analogous to the incoherent co-polar discrimination (I-CPD), introduced by Ishimaru *et al.* [22]. Neglecting the radiation pattern effects, by definition

zero IPD values correspond to $\tau_{\rm A} = -\tau_{\rm Ai} = ln2 - \tau_{\rm At}$. IPD negative values are indicators of the predominance of incoherent effects at the receiving antenna location.

IV. Numerical Results

In order to simulate a realistic earth–satellite link, we need to specify the receiving antenna radiation pattern to compute (20). The receiving antenna has been assumed to be a paraboloid of revolution with a diameter $D_{\rm A}$ of 1.5 m. The approximate expression for the semi-angle $\theta_{\rm A}$ of the antenna beamwidth is derived from $\theta_{\rm A} \cong 29(\lambda/{\rm D_A})$, where $\theta_{\rm A}$ is in degrees, $D_{\rm A}$ in meters and λ [m] is the free-space wavelength [44]. The previous expression holds for a paraboloid with uniform illuminated aperture, considered equivalent to a circular aperture of the same diameter $D_{\rm A}$ in an infinitely extending absorbing screen with a uniform plane wave incident on it. For a tapered illumination, $\theta_{\rm A}$ would be larger. For the considered frequency bands, $\theta_{\rm A}$ is equal to 0.37°, 0.23°, 0.18°, and 0.14° at 20, 30, 40, and 50 GHz, respectively.

Six different values of rain rate R (i.e., 1, 5, 12, 25, 50, and 100) have been considered and, for each R value, a set of hydrometeor profiles has been arbitrarily selected within the entire cloud model grid. All simulations have been performed at two elevation angles $\theta_{\rm e}$ equal to 20° (or $\theta = 70°$) and to 40° (or $\theta = 50°$), even though only results at 40° elevation angle will be shown in this work. All RT simulations have been then performed in the incident azimuthal plane $\phi = \phi_0$.

The guideline of the following sensitivity analysis is to show the variability of total attenuation and the impact of multiple scattering on slant paths when going from simple rain-slab models to more realistic three-dimensional precipitating clouds. Section IV-A deals with a single homogeneous layer characterized by the presence of rain (i.e., a rain slab). For each selected pixel, only the rain layer closest to the ground has been considered and its rain content uniformly extended to the slab height. In Section IV-B the atmospheric model is extended to take into account the vertical stratification of the atmosphere associated to a single pixel, considered as a plane parallel atmosphere. This assumption is more realistic than the rain-slab model, even though it still shows some limitations. These limitations are due to the characteristics of the layers intercepted by the coherent down-welling radiation on a slant path. In Section IV-C, using the modified plane parallel model, a line is ideally traced from the ground receiving point along the satellite-link direction through the cloud model. The grid cells of the cloud model intercepted by the line are identified and an equivalent plane-parallel atmospheric model is built by stacking the intercepted cells. This method allows for a fairly accurate computation of the received intensity and can approximately take into account the 3-D effects of the multiple scattering mechanism [36], [37].

Hereinafter we will show results of path attenuation up to 100 dB. However, it should kept in mind that current available carrier-to-noise (C/N) values in the 20–50 GHz band are less than 55 dB [4]. For instance, a typical link budget for the ITALSAT main stations gives rise to a nominal dynamic range of 40.8, 46.9, and 40.9 dB for the 20-, 40-, and 50-GHz beacons, respectively [29].

A. Homogeneous Rain Slab

The height H of the rain slab has been set to 5 km. Indeed, the effective rain height H, as suggested by the International Telecommunication Union (ITU-R), is given by $H = 5$ km for $0° \leq \gamma \leq 23°$ where γ is the latitude [11]. As apparent from Fig. 1, the ITU-R slab-height value of 5 km is in a fairly good agreement with the freezing level height of the considered cloud-model simulation carried out for a subtropical region. For each selected surface rain rate, eight rain profiles have been considered. Corresponding eight rain slabs of 5-km thickness have been generated by imposing, as a rain slab content, the rain amount of the profile layer closest to the surface. The choice of considering eight samples has been dictated by the availability of only 1 min simulation and by the aim to guarantee the same number of slabs for each R value. The final results have been obtained by computing the mean and minimum values of each sensitivity parameter, defined in Section III-B.

The top panels of Fig. 3 show the mean coherent attenuation $A_{\rm c}$, defined in (24), and the coherent attenuation $A_{\rm c}$, derived from the Recommendation ITU-R P.838-1 [11], as a function of surface rain rate for four frequencies at 20, 30, 40, and 50 GHz for an elevation angle of 40°. At 50 GHz total path attenuation is already larger than 50 dB for $R > 15$ mm/h. Even though not shown, at 40° elevation $A_{\rm c}$ can reach values up to 225 dB at 50 GHz for $R = 100$ mm/h. Notice that the rain paths for an elevation of 40° and 20° are of 7.8 and 14.6 km, respectively.

Our calculations for $A_{\rm c}$ are consistent with the ITU-R ones, a fact which is not surprising since ITU-R model also utilizes a Laws–Parsons inverse-exponential HSD assuming spherical raindrops [11]. At higher frequencies a discrepancy up to 10 dB may be also noted. This difference is due to: 1) the averaging process of eight different rain-slab results derived from the cloud model; 2) the use of Marshall–Palmer HSD parameters only for the intercept N_0 and not for the logarithmic slope Λ (see Section III-A); and 3) the impact of the drop terminal velocity (taken into account at each grid point of the cloud model) on the calculation of the surface rain rate. The latter consideration has the consequence that the relation between rain amount and surface rain-rate can be spatially variable and can affect the rain-slab averaging process. This contrasts with methods based on Mie scattering computations, such as ITU-R, which avoid this intermediate step by identifying surface rain rate with HSD exponent parameter (as in the case of Marshall–Palmer or Laws–Parson HSDs) [10].

It is worth mentioning that, from previous analyses [26], it emerges that at 40° elevation the first-order scattering approximation can be acceptable for R less than 50 mm/h and any frequency, while at 100 mm/h and at V-band $\rho_{\rm TF}$ [given in (27)] becomes less than 90%. At 20° elevation, the ratio $\rho_{\rm TF}$ becomes already less than 90% for $R > 40$ mm/h at 30 GHz and for $R > 20$ mm/h at 50 GHz. In these cases higher-order scattering should be included in the RT solution [46], e.g., using FEM described in Section II-C.

A sensitivity parameter, useful for quantifying the differences between $A_{\rm c}$ and $A_{\rm t}$, is the incoherent-to-total attenuation ratio $\rho_{\rm IT}$, defined in (26), and the mean IPD, defined in (28). Middle panels of Fig. 3 shows IPD and $\rho_{\rm IT}$ as a function of surface rain

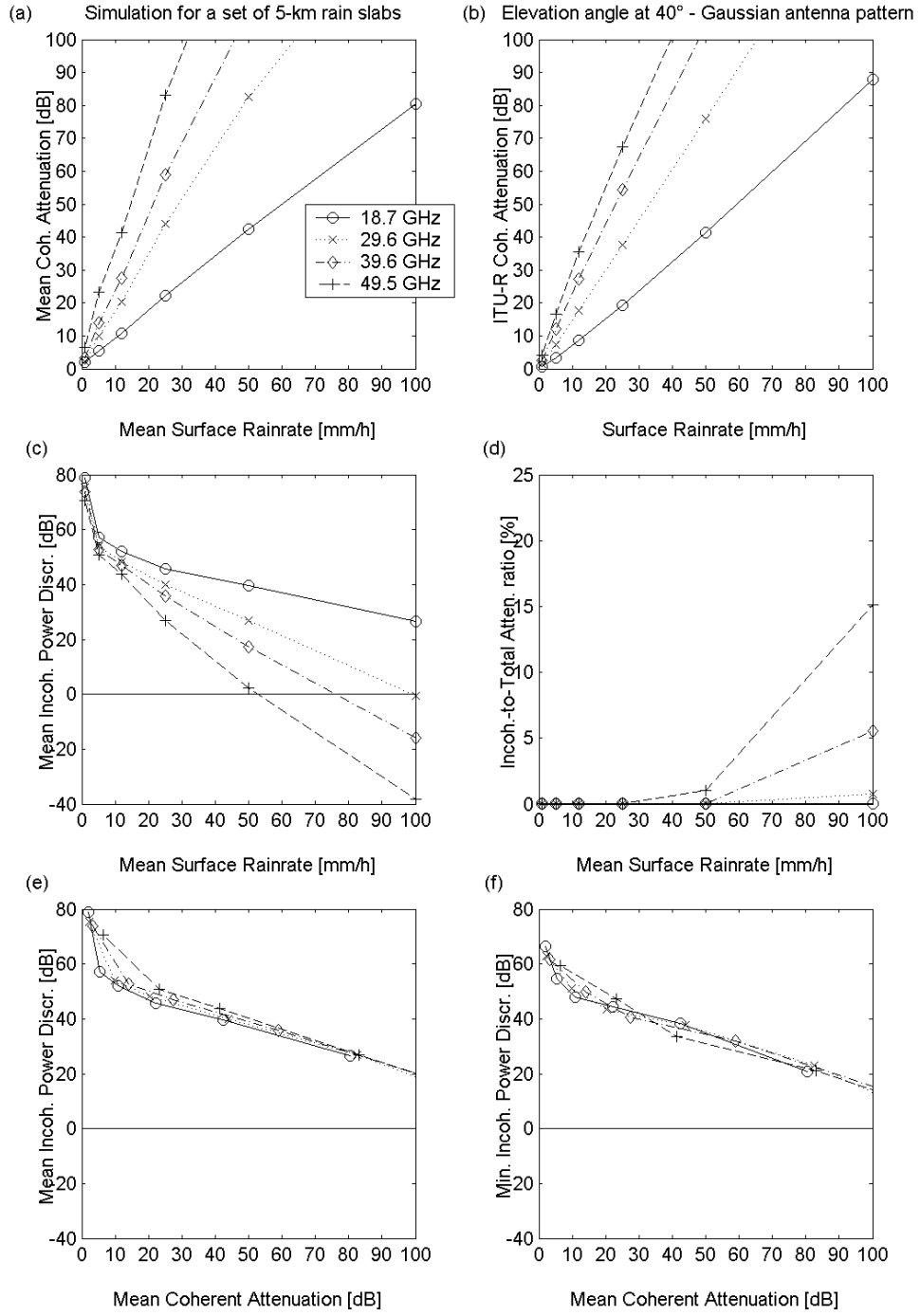

Fig. 3. (a) Mean coherent attenuation A_c, defined in (41) as a function of surface rain rate R. (b) Coherent attenuation A_c, derived from Recommendation ITU-R P.838-1, as a function of R. (c) Mean incoherent power discrimination IPD, defined in (43), as a function of R. (d) Incoherent-to-total attenuation ratio ρ_{IT}, defined in (41) as a function of R. (e) Mean IPD as a function of mean A_c. (f) Mean IPD as a function of mean coherent attenuation A_c. All numerical results refer to four frequencies at 20, 30, 40, and 50 GHz and to an elevation angle at 40°. ITU-R results are derived for a homogeneous slab of 5-km height, while mean and minimum values of considered definitions (see Section III-B) are obtained, for each rain rate, by averaging the results of eight rain slabs of 5-km height having the same R. Values of IPD and A_c are cut to -40 and 100 dB, respectively. IPD line at 0 dB is also plotted for comparison.

rate at 20, 30, 40, and 50 GHz and for an elevation angle of 40°. The IPD results can be also shown as a function of the coherent attenuation: this representation gives an indication about the possible detection of incoherent scattering effects in terms of the actual dynamic range of a receiver. Bottom panels of Fig. 3 show the mean and the minimum of IPD, as a function of mean coherent attenuation A_c, at 20, 30, 40, and 50 GHz and for an elevation angle of 40°.

Even though ρ_{IT} can be higher than 100% at 40° and for frequencies higher than 30 GHz, when considering coherent attenuation less than 50 dB, we realize that incoherent attenuation is generally less than 15% at 40° (and less than 25% at 20°). Minimum IPD values are lower than mean IPD values, especially for $A_c \leq 20$ dB, denoting an appreciable variability within the set of chosen rain slabs. The IPD analysis parameter has been largely used by Ishimaru *et al.* [22] to plot multiple scattering

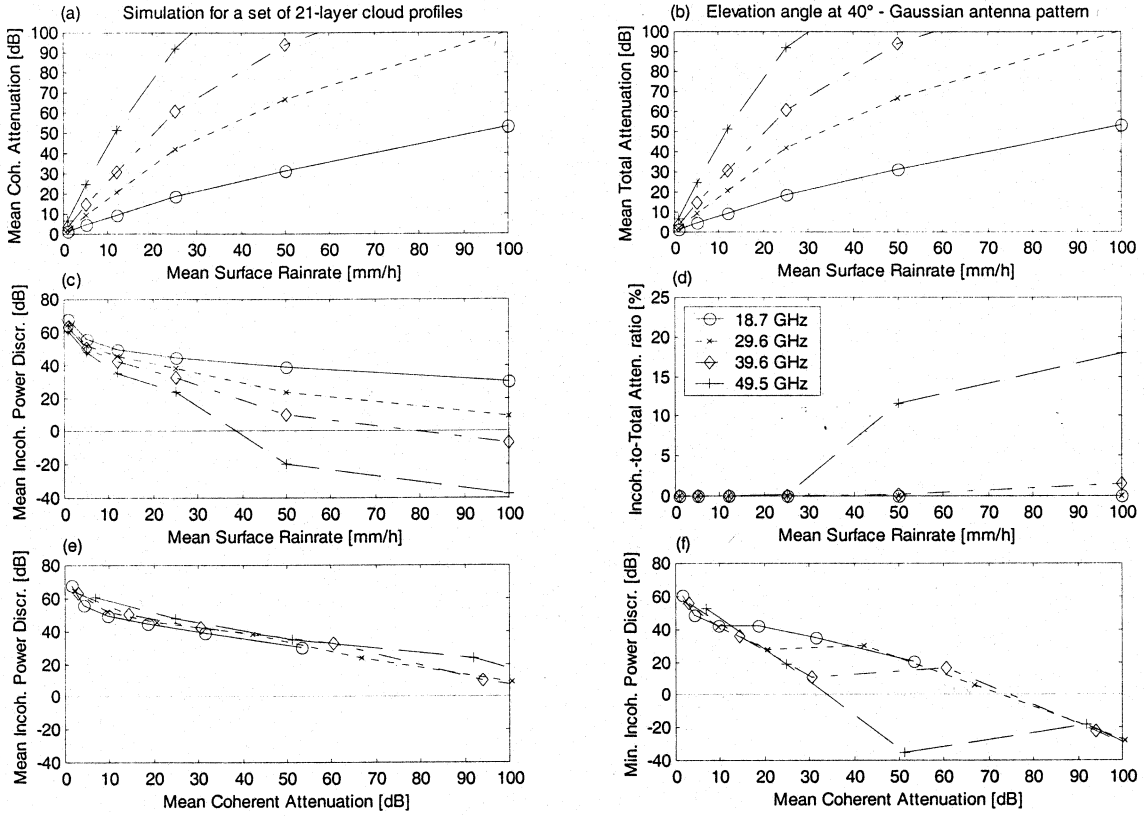

Fig. 4. (a) Mean coherent attenuation A_c as a function of surface rain rate R. (b) Mean total attenuation A_t as a function of R. (c) Mean incoherent power discrimination IPD as a function of R. (d) Incoherent-to-total attenuation ratio ρ_{IT} as a function of R. (e) Mean IPD as a function of mean coherent attenuation A_c. (f) Mean IPD as a function of mean Ac. All numerical results refer to four frequencies at 20, 30, 40, and 50 GHz and to an elevation angle at 40°. Mean and minimum values of considered definitions are obtained, for each rain rate, by averaging the results of eight vertically stratified GCE cloud profile having the same R and including cloud liquid, ice graupel and snow hydrometeors. Values of IPD and A_c are cut to -40 and 100 dB, respectively. IPD line at 0 dB is also plotted for comparison.

rain calculations of rain effects. For a rain slab of 3 km, $\theta_A = 1°$, a Laws–Parsons HSD and an elevation angle of 30°, they obtained values of IPD equal to about 20 dB at 30 GHz and to about -8 dB at 60 GHz for $\mathrm{R} = 50$ mm/h. Considering Fig. 3(c), for the same R values we have obtained IPD equal to 30 and 0 dB, respectively: differences are due to different model assumptions and basically explained by considering that the larger rain slab height is compensated by the cloud-model HSDs which tend to significantly reduce the volumetric albedo for a given R. Consistently with what found here for mean values, in [22] they did not find negative values of IPD for $A_c \leq 100$ dB, for frequencies up to 50 GHz and for elevation angles greater than 30°.

B. Vertically Inhomogeneous Raining Cloud

The next step in atmospheric modeling is to consider the entire atmospheric column associated to a pixel with a given rain rate. This type of modeling allows one to take into account the vertical stratification of the rainy cloud, including precipitating and nonprecipitating ice, as shown in Fig. 1. For each value of rain rate, the mean and minimum values of the sensitivity parameters are derived from the eight corresponding pixels in the cloud grid domain, as in Section IV-A.

The top panels of Fig. 4 show the mean coherent A_c and total A_t path attenuation obtained, for each rain rate, by averaging the results of eight vertically-stratified GCE cloud profile having the same surface rain rate. With respect to the rain-slab results of Fig. 3, the coherent attenuation significantly decreases (up to 20 dB) for $R > 50$ mm/h when considering a realistic vertically-inhomogeneous profile. This decrease is much more evident for total attenuation due to stronger incoherent effects originated from the graupel layers. It is worth noting that, even though ice graupel tends to augment coherent attenuation because of its optical thickness at Ka-band and above (see Fig. 2), this increment does not compensate for the reduction of rain-profile attenuation (due to its layered inhomogeneity) with respect to the uniform slab case.

The increased incoherent effects at V-band are confirmed by middle and bottom panels of Fig. 4, which show the same as in corresponding panels of Fig. 3. At 40° incoherent effects are in percentage less than 20% for all frequencies, while at 20° (not shown) this is true only for $\mathrm{R} < 25$ mm/h reaching values of 100% for $R = 100$ mm/h at V-band.

Mean IPD values show appreciable incoherent effects only for $\mathrm{R} > 50$ mm/h at 50 GHz being slightly less than corresponding IPD values due to rain slabs. For $A_c \leq 100$ dB mean IPD is always positive. On the contrary, minimum IPD values are less than 0 dB for $A_c \leq 50$ dB at V-band and much more disperse than in the case of rain slabs, denoting the impact of vertical profile variability.

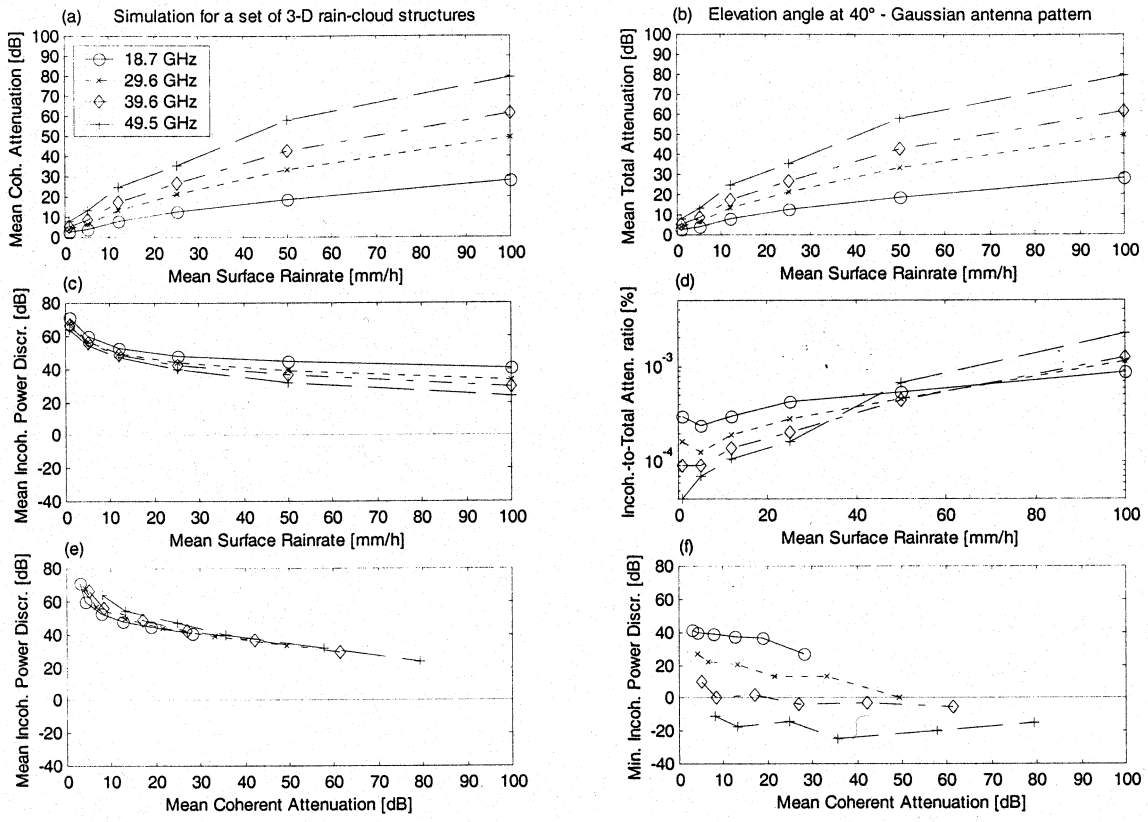

Fig. 5. Same as in Fig. 4, but for results obtained, for each rain rate, by averaging the results of eight vertically-stratified GCE cloud profile having the same surface rain rate and including cloud liquid, ice graupel, and snow hydrometeors.

C. Vertically and Horizontally Inhomogeneous Raining Clouds

For each selected rain rate value, eight pixels have been considered and our antenna azimuthal viewing angles (i.e., 0°, 90°, 180°, and 270°) have been selected. For each pixel a line has been traced from the ground in the four satellite-link directions. The scattering parameters of the grid cells, intercepted by each line-of-sight (inclined column), have been used to create a plane-parallel raining cloud structure. The mean and minimum values of sensitivity analysis parameters have been computed, as in previous sections. Note that in this case the ensemble average, for each R, has been carried out on 32 values (eight profiles by four azimuthal angles).

Fig. 5 shows the same as in Fig. 4, but for results obtained, for each rain rate, by averaging the results of the eight inclined profiles having the same surface rain rate and elevation angle (with inclination equal to the elevation angle) with four different azimuthal angles. It is evident the large reduction of both coherent and total attenuation values, as compared to those obtained in case of rain slabs and hydrometeor vertical profiles (see Figs. 3 and 4). For a given R, $A_{\rm c}$, and $A_{\rm t}$ can be even halved reaching values of no more than 80 dB. Up to 50 mm/h, $A_{\rm c}$ at V-band is less than 50 dB.

The reduction of path attenuation and volumetric albedo causes incoherent contribution to be strongly decreased with mean values of IPD always larger than 0 dB at 40° for any frequency and rain rate. The most interesting feature is the impact of considering the minimum values of IPD. At 40°, where mean IPD was always greater than zero, minimum IPD is negative at V-band for $A_{\rm c}$ less than 50 dB. At 20° elevation minimum IPD values (not shown) are almost constant with $A_{\rm c}$ and are significantly negative at Ka-band and above. This means that in the worst cases the surface rain rate dependency of total path attenuation appears to be much lower than the frequency dependency.

This behavior can be understood by realizing that a receiver with a given elevation angle, but at different azimuthal angles, can detect very different incoming radiation, depending on the crossed cloud volumes along the line-of-sight. In case of a line-of-sight intercepting the convective cloud core, path attenuation values are expected to be higher than those obtained from the same position at the ground and the same elevation, but with a line-of-sight mainly intercepting the stratiform rain region or the ice anvil of the cloud. This viewing effect is more evident for low elevation angles, because the precipitation path is longer and, therefore, the probability on intercepting a convective portion of the cloud is higher. This situation can be visualized by considering Fig. 1 where for a surface rain rate of 10 mm/h (around x = 25 km or x = 35 km), the line-of-sights (belonging to the cross-section plane) between 20° and 40° elevation angles would intercept the regions with rain and/or graupel highest concentration.

V. Conclusion

A numerical investigation has been carried out in order to evaluate the impact of a realistic rainfall cloud model on microwave attenuation along earth–satellite low-elevation links in

20–50-GHz band. The analysis has been accomplished both for coherent attenuation, due to absorption and in-phase forward scattering inside the medium, and for the incoherent component of the received field, due to hydrometeor multiple scattering processes.

Mie scattering computations, applied to a cross-section of a 3-D hydrometeor profile grid under the spherical particle-shape assumption, have shown the increasing importance of ice graupel as frequency becomes higher than 30 GHz. The scattering effects have been evaluated in terms of both specific attenuation, volumetric albedo and asymmetry factor, showing that the latter two are dominated by ice graupel presence.

The choice of a radiative transfer approach has enabled the analysis of any order of scattering within the medium. Theoretical relations of the RT theory with the wave theory, founded on the Twerskii integral equations, has been briefly outlined. Within this electromagnetic propagation model, the forward coherent multiple scattering effect has been rigorously derived and shown to be described by radiative transfer theory as well. An efficient and accurate radiative transfer algorithm, based on the FEM, has allowed us to compute the received specific intensity supposing a collimated beam at the satellite transmitter. The received specific intensity has been integrated over an approximate antenna radiation pattern to calculate the received power. The beamwidths at K-band and above have been specified for paraboloid antennas of 1.5-m diameter. First order scattering has been numerically proved to be suitable at V-band only for elevation angles higher than 40°.

The RT algorithm has been applied first to a rain slab, then to a 21-layer vertically stratified cloud profile including four hydrometeor species and, finally, to a precipitating-cloud structure inclined along the line-of-sight. By taking eight profiles for each surface rate between 0 and 100 mm/h, we have evaluated the results in terms of mean and minimum values of coherent and incoherent path attenuation and in terms of the incoherent power discrimination parameter IPD. In this context the results relative to the minimum values can be interpreted as the worst case for earth–satellite propagation. Beacon frequencies of OLYMPUS and ITALSAT at K-band and above together with two elevation angles at 20° and 40° have been considered.

It has been proved that rain slab models denote significant limitations due to the fact that spatial variability and precipitating ice scattering is not taken into account. These effects can be considered by modeling the rainy cloud by means of a vertically-stratified medium. Ice graupel contributes to both coherent and incoherent attenuation, even though the total path attenuation can be still comparable with the rain slab one due to the considered profile inhomogeneity. Minimum IPD values can be less than 0 dB for coherent path attenuation less than 40 dB at V-band.

Three-dimensional aspects of the path attenuation and multiple scattering problem can lead to surprising effects. Mean coherent and total attenuation are strongly reduced with respect to rain slab and cloud profile cases, basically due to the viewing geometry of the inclined line-of-sight. Coherent path attenuation can be even half than that obtained from both rain slab and vertical profile models. Even though mean IPD values are less than those of the other two atmospheric models, at 40° elevation angle minimum IPD becomes negative for coherent attenuation larger than even 10 and 30 dB at Ka- and V-band, respectively. Results for 3-D realistic clouds have shown that the total path attenuation can exhibit a rain rate dependence much less than the frequency one in the worst cases.

From this numerical study it can be concluded that the impact of the chosen atmospheric model can be significant both in determining the total attenuation and to quantify the multiple scattering contribution to the received power. For intense rainfall along low elevation-angle links, the use of a rain slab model can overestimate coherent attenuation and, at the same time, underestimate incoherent intensity. Total path attenuation can strongly depend on the pointing direction of the receiving antenna due to the intrinsic variability of cloud composition along the slant path. Even though affected by uncertainty on the underlined microphysics and dynamics assumptions, cloud-resolving 3-D models can represent a valuable data sources which could be used to carry out model analyses and to develop rainfall prediction techniques in the same way as already accomplished using weather radar data. The results shown here refer to a particular numerical case study, carried out by using the 3-D outputs of a single time step of a cloud-resolving model. Further work should be devoted to prove these results by using other simulations in different climate regions.

ACKNOWLEDGMENT

The authors would like to thank Dr. C. D. Kummeorw and Dr. W.-K. Tao from NASA Goddard Space Flight Center for making the cloud model available. The comments of anonymous reviewers have been gratefully appreciated for their helpful criticism and suggestions.

REFERENCES

[1] P. A. Watson and Y. F. Hu, "Prediction of attenuation on satellite-earth links for systems operating with low fade margins," *Proc. IEE—Microwave Antennas Propagation*, vol. 141, pp. 467–472, 1994.

[2] D. V. Rogers, L. J. Ippolito Jr., and F. Davarian, "System requirements for Ka-band propagation effects on earth–satellite links," *Proc. IEEE*, vol. 85, pp. 810–821, June 1997.

[3] S. M. R. Jones and P. A. Watson, "Attenuation and countermeasures in millimeter-wave point-to-multipoint networks," *Radio Sci.*, vol. 28, pp. 1057–1069, 1993.

[4] B. R. Arbesser-Rastburg and A. Paraboni, "European research on Ka-band slant path propagation," *Proc. IEEE*, vol. 85, pp. 843–852, June 1997.

[5] M. Filip and E. Vilar, "Optimum utilization of the channel capacity of a satellite link in the presence of amplitude scintillations and rain attenuation," *IEEE Trans. Commun.*, vol. COM-28, pp. 1958–1965, Nov. 1990.

[6] R. K. Crane, "Prediction of attenuation by rain," *IEEE Trans. Commun.*, vol. 28, pp. 1717–1733, Sept., 1980.

[7] L. J. Ippolito, "Radio propagation for communications," *Proc. IEEE*, vol. 69, pp. 697–727, June 1981.

[8] R. L. Olsen and M. M. Z. Kharadly, "Experimental investigation of the scattering of electromagnetic waves from a model random medium of discrete scatterers," *Radio Sci.*, vol. 11, pp. 39–48, 1976.

[9] D. Maggiori, "Computed transmission through rain in the 1–400 GHz frequency range for spherical and elliptical drops and any polarization," *Alta Freq.*, vol. L, pp. 262–273, 1981.

[10] R. L. Olsen, D. V. Rogers, and D. B. Hodge, "The aR^b relationship in the calculation of rain attenuation," *IEEE Trans. Antennas Propagat.*, vol. 26, pp. 318–329, Feb. 1978.

[11] ITU-R Recommendation P.838-1, "Specific attenuation model for rain for use in prediction methods," *Int. Telecomm. Union—Radiocomm. (ITU-R) Recommendations*, ser. P, pt. 1, pp. 1–50, 1999.

[12] F. S. Marzano, J. Turk, P. Ciotti, S. Di Michele, and N. Pierdicca, "Potential of combined spaceborne infrared and microwave radiometry for near real-time rainfall attenuation monitoring along earth-satellite links," *Int. J. Satellite Commun.*, vol. 19, no. 4, pp. 385–412, 2001.
[13] M. J. Leitao and P. A. Watson, "Method for prediction of attenuation on earth-space links based on radar measurements of the physical structure of rainfall," in *Proc. Inst. Elect. Eng.*, vol. 133, 1986, pp. 429–440.
[14] ——, "Application of dual linearly polarized radar data to prediction of microwave path attenuation," *Radio Sci.*, vol. 19, pp. 209–221, 1984.
[15] K. Tao, J. Simpson, and S. T. Soong, "Statistical properties of a cloud ensemble: a numerical study," *J. Atomic Sci.*, vol. 44, pp. 3175–3187, 1987.
[16] C. M. Ewenz, W. Lieff, A. S. Kulessa, and S. Salomon, "Using mesoscale models together with PEM propagation models to determine microwave link output," in *Proc. URSI Communication CLIMPARA*, Budapest, Hungary, May 28–30, 2001, pp. 89–92.
[17] G. Brussaard and P. A. Watson, *Atmospheric Modeling and Millimeter Wave Propagation*. London, U.K.: Chapman & Hall, 1995.
[18] C. Capsoni and A. Paraboni, "Properties of the forward-scattered incoherent radiation through intense precipitation," *IEEE Trans. Antennas Propagat.*, vol. AP-26, pp. 804–809, Nov. 1978.
[19] C. Capsoni, M. Mauri, and A. Paraboni, "Incoherent effects in electromagnetic propagation through rain," *Ann. Telecommun.*, vol. 32, pp. 409–414, 1977.
[20] T. Oguchi, "Effect of incoherent scattering on attenuation and cross-polarization of millileter waves due to rain: preliminary calculations at 34.8 and 82 GHz for spherical raindrops," *Ann. Telecommun.*, vol. 35, pp. 380–389, 1980.
[21] A. Ishimaru and R. L.-T. Cheung, "Multiple scattering effects on wave propagation due to rain," *Ann. Telecommun.*, vol. 35, pp. 373–379, 1980.
[22] R. L.-T. Ishimaru, R. Woo, J. W. Armstrong, and D. C. Blackman, "Multiple scattering calculations of rain effects," *Radio Sci.*, vol. 17, pp. 1425–1433, 1982.
[23] R. L. Olsen, "A review of theories of coherent radio wave propagation through precipitation media of randomly oriented scatterers, and the role of multiple scattering," *Radio Sci.*, vol. 17, pp. 913–928, 1982.
[24] T. Oguchi, "Electromgnetic wave propagation and scattering in rain and other hydrometeors," *Proc. IEEE*, vol. 71, pp. 1029–1078, Sept. 1983.
[25] ——, "Effects of incoherent scattering on attenuation and depolarization of millimeter and optical waves due to hydrometeors," *Radio Sci.*, vol. 21, pp. 717–730, 1986.
[26] L. Roberti and F. S. Marzano, "Analysis of multiple scattering effects upon space-earth rain attenuation at Ku band and above," in *Proc. IEE Conf. Antennas and Propagation (ICAP-2000)*, Davos, Switzerland, Apr. 10–14, 2000, pp. 1–4.
[27] A. Ishimaru, *Wave Propagation and Scattering in Random Media*. New York: Academic, 1978, vol. 1 and 2.
[28] T. Oguchi, "Effects of incoherent scattering on microwave and millimeter wave communications through rain," *Electron. Lett.*, vol. 27, pp. 759–760, 1991.
[29] R. Polonio and C. Riva, "ITALSAT propagation experiment at 18.7, 39.6, and 49.5 GHz at Spino d'Adda: three years of CPA statistics," *IEEE Trans. Antennas Propagat.*, vol. 46, pp. 631–635, May 1998.
[30] A. Ishimaru, "Correlation functions of a wave in a random distribution of stationary and moving scattering," *Radio Sci.*, vol. 10, pp. 45–52, 1975.
[31] V. Twersky, "On scattering of waves by random distributions. I. Free space scatterer formulation," *J. Math. Phys.*, vol. 3, pp. 700–715, 1962.
[32] K. N. Liou, *An Introduction to Atmospheric Radiation*. New York: Academic, 1980.
[33] E. Wolf, "Coherence and radiometry," *J. Opt. Soc. Amer.*, vol. 68, pp. 6–17, 1978.
[34] Y. A. Kratsov and L. A. Apresyan, "Radiative transfer: new aspects of the old theory," in *Progress in Optics*, E. Wolf, Ed. Amsterdam, The Netherlands: Elsevier, 1996, vol. 36, pp. 200–212.
[35] B. Wen, L. Tsang, D. P. Winebrenner, and A. Ishimaru, "Dense medium radiative transfer theory: comparison with experiment and application to microwave remote sensing and polarimetry," *IEEE Trans. Geosci. Remote Sensing*, vol. 28, pp. 46–59, Jan. 1990.
[36] L. Roberti, J. Haferman, and C. Kummerow, "Microwave radiative transfer through horizontally inhomogeneous precipitating clouds," *J. Geophys. Res.*, vol. 99, pp. 16 707–16 718, 1994.
[37] Q. Liu, C. Simmer, and E. Ruprecht, "3-D Radiation transfer effects of clouds in the microwave spectral range," *J. Geophys. Res.*, vol. 101 D2, pp. 4289–4298, 1996.
[38] F. S. Marzano, E. Fionda, and P. Ciotti, "Simulation of radiometric and attenuation measurements along earth-satellite links in the 10 to 50 GHz band through horizontally-finite convective raincells," *Radio Sci.*, vol. 39, pp. 841–858, 1999.
[39] K. Stamnes, S. Tsay, W. Wiscombe, and K. Jayaweera, "Numerically stable algorithm for discrete-ordinate-method radiative transfer in multiple scattering and emitting layered media," *Appl. Opt.*, vol. 27, pp. 2502–2509, 1988.
[40] V. B. Kisselev, L. Roberti, and G. Perona, "An application of the finite element method to the solution of the radiative transfer equation," *J. Quant. Spectrosc. Radiat. Transf.*, vol. 51, pp. 603–614, 1994.
[41] ——, "A finite element algorithm for radiative transfer in vertically inhomogeneous media: numerical scheme and applications," *Appl. Opt.*, vol. 34, pp. 8460–8471, 1995.
[42] H. Liebe, "An atmospheric millimeter-wave propagation model," *Int. J. Infrared Millim. Waves*, vol. 10, pp. 367–378, 1989.
[43] A. Gasiewskii, "Microwave radiative transfer in hydrometeors," in *Atmospheric Remote Sensing by Microwave Radiometry*, M. A. Jansen, Ed. New York: Wiley, 1993, ch. 4.
[44] R. Chatterjee, *Antenna Theory and Practice*. New York: Wiley, 1988.
[45] P. Bauer, L. Schanz, and L. Roberti, "Correction of three-dimensional effects for passive microwave remote sensing of convective clouds," *J. Appl. Meteor.*, vol. 37, pp. 1619–1632, 1998.
[46] D. A. de Wolf, H. W. J. Russchenberg, and L. P. Ligthart, "Radar reflection from clouds: gigahertz backscatter cross sections and doppler spectra," *IEEE Trans. Antennas Propagat.*, vol. 48, pp. 254–259, Feb. 2000.

Frank Silvio Marzano (S'88–M'99–SM'03) received the Laurea degree (*cum laude*) in electronic engineering and the Ph.D. degree in applied electromagnetics from the University "La Sapienza" of Rome, Rome, Italy, in 1988 and 1993, respectively.

In 1992, he was a Visiting Scientist at Florida State University, Tallahassee, and in 1993 he collaborated with the Institute of Atmospheric Physics, CNR, Rome, Italy. From 1994 to 1996, he was a Postdoctoral Researcher with the Italian Space Agency, Rome, Italy. From 1996 to 1997, he was a Lecturer at the University of Perugia, Perugia, Italy. In 1997, he joined the Department of Electrical Engineering and the Center of Excellence CETEMPS at the University of L'Aquila, L'Aquila, Italy, teaching courses on antennas and propagation and coordinating the satellite and radar group. His research concerns passive and active remote sensing of the atmosphere from ground-based, airborne, and spaceborne platforms, inversion methods, radiative transfer modeling of scattering media, and tropospheric scintillation and rain fading analysis along satellite-earth microwave links.

Dr. Marzano received the Young Scientist Award at the XXIV General Assembly of the International Union of Radio Science (URSI) in 1993 and the Alan Berman Research Publication Award (ARPAD) from NRL, Washington, DC, in 1993. Since 2001, he has been a national delegate within the COST-280 European action.

Laura Roberti (M'01) received the degree in mathematics (*cum laude*), the degree in electronic engineering (*cum laude*), and the Ph.D. degree in electronic engineering from the Politecnico of Turin, Turin, Italy, in 1992, 1996, and 1998, respectively.

She was a Visiting Scientist at NASA Goddard Space Flight Center, Greenbelt, MD, for one year. In 1995, she was an Assistant Professor with the Department of Electronics, Politecnico of Turin, working on a number of research projects on radiative transfer and atmospheric remote sensing. Since 1997, she has been at British Telecom Laboratories, Ipswich, U.K., working on aspects related to microwave propagation along earth–space paths.